ACS APPLIED MATERIALS & INTERFACES

Research Article

www.acsami.org

Tuning Activities of $K_{1.9}Na_{0.1}Ta_2O_6{\cdot}2H_2O$ Nanocrystals in Photocatalysis by Controlling Exposed Facets

Yingxuan Li,[†] Shuai Chen,[†,‡] Hongquan He,[†,‡] Ying Zhang,[†,‡] and Chuanyi Wang*[,†]

[†]Laboratory of Environmental Sciences and Technology, Xinjiang Technical Institute of Physics & Chemistry; Key Laboratory of Functional Materials and Devices for Special Environments, Chinese Academy of Sciences, Urumqi 830011, China

[‡]University of Chinese Academy of Sciences, Beijing, 100049, P.R. China

ABSTRACT: Morphology-controlled synthesis of tantalates is a major challenge in the field of material science. Herein, an innovative strategy has been developed for controllably synthesizing $K_{1.9}Na_{0.1}Ta_2O_6{\cdot}2H_2O$ (KNTO) nanocrystals shaped as octahedra and nanosheets without using any capping agents. The obtained nanocrystals show high activity in photocatalytic H_2 evolution from CH_3OH/H_2O solution, and their performance closely depends on the exposed facets, in which the {111}-facet-bounded nanooctahedra exhibit more than 3 times higher activity than the nanosheets dominated with {101} facets. The influence of surface atomic structure and electronic band structure on the photocatalytic properties of the KNTO nanocrystals is systematically studied. This is the first report for the facet controllable synthesis of tantalate materials with highly regular shapes. The present approach is anticipated as a general strategy for controllable synthesis of tantalate materials and also provides feasibility for rational design and activity optimization of shape-controlled photocatalysts for H_2 production.

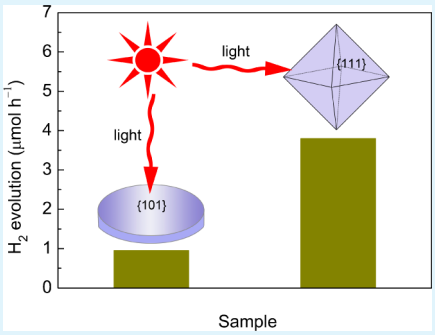

KEYWORDS: *$K_{1.9}Na_{0.1}Ta_2O_6{\cdot}2H_2O$, nanooctahedra, nanosheets, photocatalytic H_2 evolution, exposed facets, surface structure*

1. INTRODUCTION

Morphology-controlled synthesis of inorganic nanocrystals has attracted intense research interest for the purpose of tuning their physical and/or chemical properties.[1−4] In particular, rational design and morphological control of exposed crystal facets of photocatalysts have become one of the most effective strategies to optimize their performance since the pioneering work of Yang et al.[5] From this prospect, numerous recent publications have reported controllable synthesis of single crystalline photocatalysts exposed with optimized reactive facets.[6−12] Unfortunately, only a limited number of photocatalysts with crystal-facet-dependent activities were successfully fabricated. In addition, most of the past reports focused on the influences of crystalline facets on the activities for pollutant degradation or O_2 evolution from water splitting.[6−12] To the best of our knowledge, except for TiO_2,[13−16] the relationship between exposed facets and activities for H_2 production has been rarely studied, although over 130 inorganic photocatalysts have been discovered for water splitting.[17] Therefore, crystal facet-controlled synthesis deserves to be explored as a potential route for fabricating new generation photocatalysts with high activity for H_2 production. As reported,[6,13] capping agents are usually employed in synthesizing crystals with different facets, which is unfavorable for the catalytic applications because many surface active sites may be lost in the process of removing the capping agents by complex treatments. Consequently, a facile and capping-agent-free strategy for the facet-controlled fabrication of catalysts is highly desirable.

Recently, tantalates have been extensively studied due to their high photocatalytic activities for splitting water into H_2.[18−23] However, the tantalates are usually synthesized by solid state methods at high temperature of around 1000 °C over long periods,[18−23] which may result in large grain growth (thus reduction in surface areas), leading to a decrease in photocatalytic activity.[24] So far, only a few types of tantalates, such as $Sr_2Ta_2O_7$,[22] $ATaO_3$ (A = Li, Na, K),[23] $Ba_5Ta_4O_{15}$,[25] $BaTa_2O_6$,[26] etc., have been synthesized by a hydrothermal method at much lower temperature. However, crystal-facet-controlled synthesis of tantalates still remains a challenge and has hitherto never been reported. Herein, we report for the first time on the facile synthesis of $K_{1.9}Na_{0.1}Ta_2O_6{\cdot}2H_2O$ (KNTO) nanocrystals with controllable crystalline facets by a novel two-step synthesis approach, namely, molten salt in combination with hydrothermal processing. This strategy is highlighted by the fact that the shape and facet controlling of KNTO is achieved by simply adjusting the concentration of KOH addition in the hydrothermal reaction. Importantly, photocatalytic activity of the synthesized KNTO for H_2 evolution from CH_3OH/H_2O solution was successfully tuned through the specific control of exposed facets.

Received: July 27, 2013
Accepted: September 11, 2013
Published: September 11, 2013

 © 2013 American Chemical Society

2. EXPERIMENTAL SECTION

Sample Preparation. Table 1 lists the experimental details for the preparation of KNTO nanocrystals with different morphologies, which

Table 1. Morphology and Composition of the KNTO Samples

sample	V_{Ta} (mL)	V_{KOH} (mL)	morphology	K/Na/Ta	surface areas (m^2 g^{-1})
1	69	1	octahedra	1.81:0.09:2	12.38
2	67.0	3.0	nanosheets	1.85:0.09:2	11.42

are defined as samples 1−2. To prepare KNTO nanooctahedra, a mixture of Ta_2O_5 (0.5 g), NaOH (3.855 g), and KOH (5.651 g) was fused at 240 °C (0.5 g) in a Teflon cup for 20 h and air-cooled to room temperature. The mixed hydroxides can be totally molten at 240 °C, which is the key for the preparation of a soluble Ta precursor. Deionized water (50 mL) was then added into the cup to dissolve the alkalis. The white product collected by centrifugation was dissolved into 100 mL of deionized water to form a clear transparent solution. Then, 1 mL of 5 M KOH aqueous solution (V_{KOH}) was added dropwise into the above clear solution (V_{Ta} = 69 mL) under constant stirring. With constant magnetic stirring for 8 h, the reaction mixture was then loaded into a 100 mL Teflon stainless autoclave which was maintained at 180 °C for 3 h and then air-cooled to room temperature to form white product. The resultant white product was collected by centrifugation, washed with deionized water for several times, and finally dried at 60 °C under vacuum. KNTO nanosheets were prepared under hydrothermal conditions at 180 °C for 1 h (V_{Ta} = 67 mL, and V_{KOH} = 3 mL).

Characterization. The crystal structures of the samples were characterized on a Bruker D8 X-ray diffractometer with Cu Kα radiation (λ = 0.15418 nm). The amounts of metals were measured by inductively coupled plasma emission spectrometry (ICP; Perkin-Elmer, Optima 5300DV) after the sample was dissolved in a mixture of HNO_3 and HF by heating at 180 °C for 3 h in a Teflon-lined stainless steel autoclave. Thermogravimetry (TG) was recorded on a NETZSCH STA 449F3 instrument. The measurement was conducted under air flow at a heating rate of 10 °C/min. The morphology photographs of the samples were taken by field emission scanning electron microscopy (FESEM; ZEISS SUPRA55VP) and transmission electron microscopy (TEM; JEOL−JEM 2100). Ultraviolet−visible (UV−vis) diffusion reflectance spectra of the samples were obtained on a SolidSpec−3700DUV spectrophotometer (Shimadzu). Brunauer−Emmett−Teller (BET) surface area of the samples was measured on a nitrogen adsorption apparatus (Micromeritics ASAP2020) at −196 °C.

Photochemical Reactions. Photocatalytic reactions were performed in a Pyrex cell with a top window, which was connected to a closed gas-circulating system. Ten mg of powdered photocatalyst was suspended by magnetic stirring in an aqueous CH_3OH/H_2O solution (10 mL of CH_3OH, 50 mL of deionized H_2O) at room temperature. An 8 W bactericidal lamp with a maximum emission at 254 nm was used as the light source. Prior to irradiation, the system was evacuated to remove the air from the system. The amount of H_2 was analyzed by an online gas chromatography (Agilent 7890A) equipped with a thermal conductivity detector (TCD). Apparent quantum yield (A.Q.Y.) of the photocatalyst was determined according to the following equation.

$$\text{A.Q.Y.}\left(\%\right) = \frac{\text{the number of reacted electrons}}{\text{the total number of incident photons}} \times 100 = \frac{\text{the number of evolved } H_2 \text{ molecules} \times 2}{\text{the total number of incident photons}} \times 100 \quad (1)$$

The light intensity for photocatalytic H_2 evolution reactions was measured using a light flux meter (1916-C, Newport) with a light sensor, and the average light intensity was ca. 1.3 mW/cm^2 at 254 nm.

3. RESULTS AND DISCUSSION

Figure 1a shows X-ray diffraction (XRD) patterns of the hydrothermally derived samples in the presence of different KOH concentrations. The XRD patterns are assigned to the pyrochlore structure of $K_2Ta_2O_6$ (PDF#00-035-1464) with space group *Fd3m*, indicating that the as-synthesized products consist of a single phase. The compositions of the two compounds determined by inductively coupled plasma (ICP) are supplied in Table 1. The atomic ratio of K/Na/Ta is close to 1.9:0.1:2. Thermogravimetry (TG) analysis of both prepared samples shows a total weight loss of ∼6.5% between room temperature and 600 °C (Figure 1b). The weight loss can be attributed to the loss of water, and the TG curves are in coincidence with the previous reports.[27,28] Combining the TG and elemental analysis above, the chemical formula of the prepared samples in this work is proposed as $K_{1.9}Na_{0.1}Ta_2O_6 \cdot 2H_2O$ (KNTO).

KNTO nanocrystals synthesized by varying the addition of 5 M KOH from 1 to 3 mL in the hydrothermal process were characterized by field-emission scanning electron microscopy, FESEM (Fugure 2). When 1 mL of 5 M KOH was added under hydrothermal conditions, octahedral nanocrystals with good uniformity are clearly observed (Figure 2a). The edge lengths of the octahedra range from 100 to 400 nm. When the volume of KOH solution was increased to 3 mL, nearly circular nanosheets with a diameter of ∼100 nm were produced (Figure

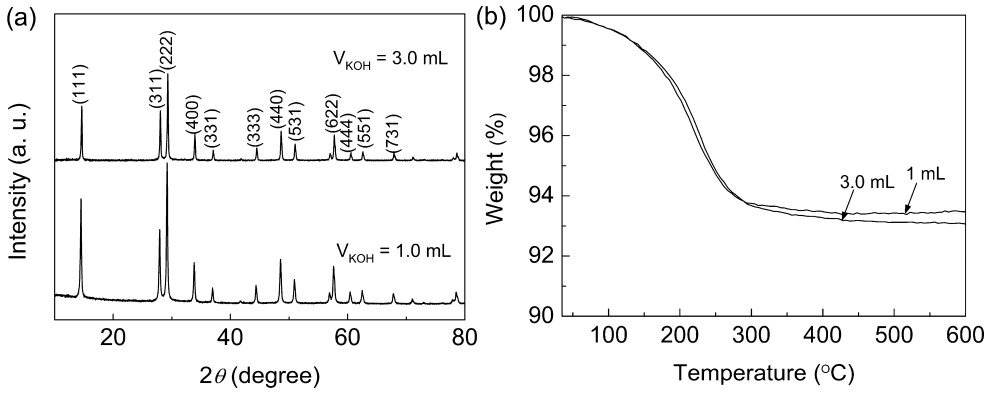

Figure 1. (a) XRD patterns and (b) TG analysis curves of the samples synthesized under different volumes of KOH added in hydrothermal reaction (V_{KOH} = 1 and 3 mL).

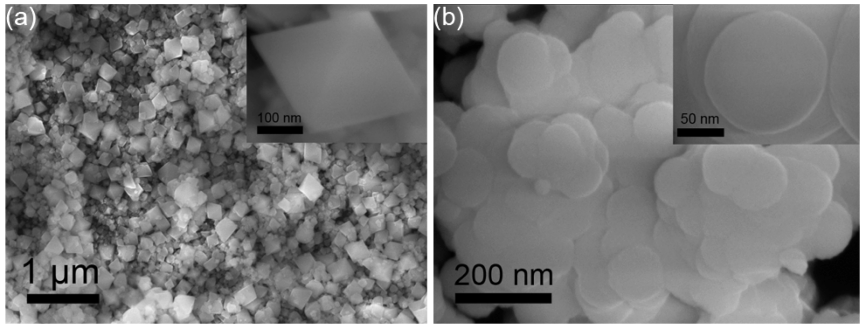

Figure 2. FESEM images of KNTO with morphologies of (a) nanooctahedra and (b) nanosheets. The insets are magnified individuals.

2b). A magnified view (inset of Figure 2b) clearly indicates that the surfaces of the nanosheets are very flat.

The morphologies and structures of the samples are further characterized by transmission electron microscopy (TEM) and selected-area electron diffraction (SAED). Figure 3 shows the

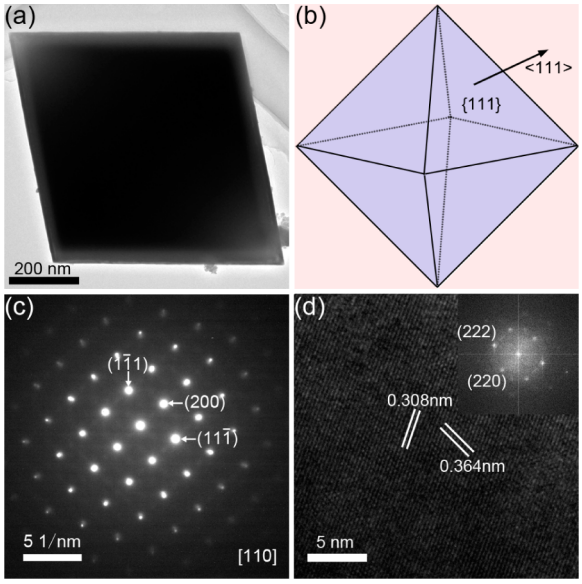

Figure 3. (a) A TEM image, (b) the schematic drawing, (c) SAED patterns, and (d) a high-resolution TEM image of the KNTO nanooctahedra.

TEM image, SAED pattern, and high-resolution TEM (HRTEM) image of a KNTO octahedron, which confirms the nature of single crystalline. The HRTEM image shows that the distance between two neighboring fringes are determined to be about 0.308 and 0.364 nm, corresponding to the (222) and (220) facets of cubic KNTO, respectively. Considering the TEM results (Figure 3) and the crystallographic symmetries of KNTO, the eight equivalent facets of the octahedron are identified as {111}.

The low-magnification TEM image in Figure 4a provides an overall morphology of KNTO nanosheets which is consistent with the FESEM image displayed in Figure 2a, while a magnified view of an individual nanosheet is shown in Figure 4b. The SAED pattern in the inset of Figure 4b shows that the nanosheet is well crystallized. The HRTEM image taken near the particle edges of the nanosheet shows lattice fringes with *d* spacings of 0.306 and 0.314 nm (Figure 4c), which correspond to the (222) and (311) lattice planes of KNTO, respectively. The fast Fourier transformation (FFT) pattern (inset of Figure

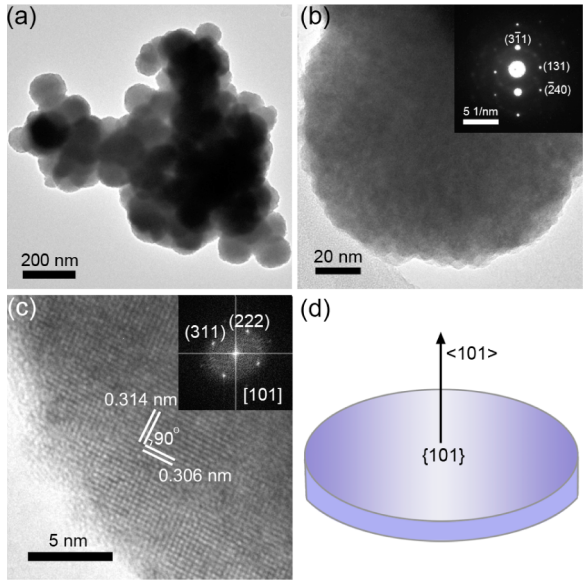

Figure 4. (a) Low-magnification TEM image, (b) high-magnification TEM image, (c) high-resolution TEM image, (d) the schematic drawing of the KNTO nanosheet. The inset of (b) is the SAED pattern of the nanocrystal. The inset of (c) is the corresponding FFT pattern of the HRTEM image.

4c) can be indexed to the [101] zone axis of KNTO. Angle analysis reveals that the measured angle between (222) and (311) facets is about 90°, which indicates that the flat surface of the disks is parallel to the (101) habit plane and the exposed facet of the KNTO nanosheet is dominated by {101} facets (Figure 4d). The above characterizations enable us to confirm that the KNTO nanooctahedra and nanosheets are dominantly exposed with {111} and {101} facets, respectively.

The XRD pattern of the sample obtained after treating in hydroxide melts can be assigned to the phase of $K_8Ta_6O_{19}\cdot mH_2O$ (PDF#21-0989) (Figure 5). On the basis of the experimental data, a possible reaction process for the formation of KNTO could be described as follows:

$$Ta_2O_5 + (K, Na)OH \rightarrow (K, Na)_8Ta_6O_{19}\cdot nH_2O \quad (2)$$

$$(K, Na)_8Ta_6O_{19}\cdot nH_2O + KOH \rightarrow K_{1.9}Na_{0.1}Ta_2O_6\cdot 2H_2O \quad (3)$$

First, the soluble $(K, Na)_8Ta_6O_{19}\cdot nH_2O$ is obtained (eq 2) by pretreating Ta_2O_5 in hydroxide melts. When the concentration of K^+ reaches or exceeds supersaturation, KNTO nuclei are formed under hydrothermal conditions (eq 3), which serve as seeds for subsequent growth into larger particles.[25]

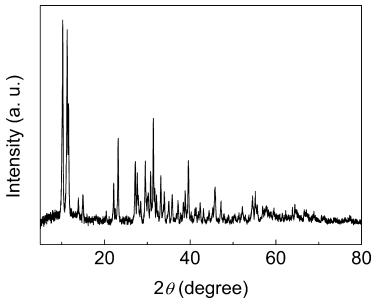

Figure 5. XRD pattern of the precursor obtained in NaOH/KOH melt at 240 °C for 20 h.

The intriguing feature of the present synthesis method is that tantalate KNTO with exposed {111} or {101} facets could be readily obtained by simply varying the amount of the KOH supplied in the hydrothermal process, indicating that the concentration of KOH plays critical roles in the crystal facet-controlled synthesis. As reported, the chemical potential of the reaction system, as a driving force for the crystal growth, is mainly determined by the concentration of KOH.[29] Theoretically, the KOH quantities can cause the transformations of the KNTO morphology and structure, which is consistent with the TEM observations. Numerous recent publications have demonstrated that the properties of single-crystalline nanocrystals are highly dependent on their surface structure.[6−16] In addition, the Ta-based materials are highly active for photocatalytic water splitting to produce H_2.[18−23] Therefore, the obtained KNTO nanocrystals with predominant {111} and {101} facets are highly beneficial for studying facet-dependent photocatalytic activity for H_2 production, which has hitherto not yet been reported.

The photocatalytic H_2 evolution on the as-prepared catalysts with different morphologies was performed under ultraviolet (UV) light irradiation (an 8W bactericidal lamp with a maximum emission at 254 nm) from an aqueous solution containing CH_3OH as a sacrificial reagent, and the results are shown in Figure 6a. Compared with the {101}-facet-enclosed

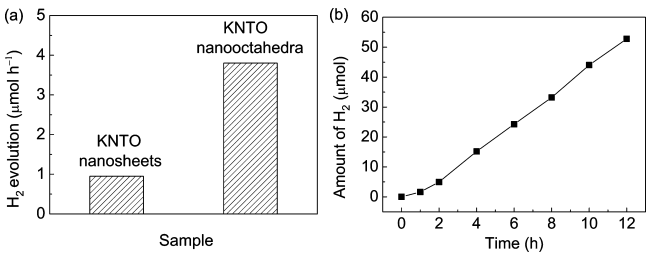

Figure 6. (a) Hydrogen evolution rate at the KNTO nanooctahedra and nanosheets under UV light irradiation in CH_3OH/H_2O solution. (b) Amounts of H_2 evolution according to reaction time of the KNTO nanooctahedra.

nanosheets, nanooctahedra exposed with dominant {111} facets show a 3 times higher activity. Figure 6b shows the reaction time course of H_2 evolution over the KNTO nanooctahedra. During the experimental period, the KNTO nanooctahedra could steadily produce hydrogen at 4.4 μmol h^{-1}. The apparent quantum yield of KNTO nanooctahedra at 254 nm is determined to be 4.7% according to eq 1. Our findings demonstrate that the present approach opens a way of facet engineering toward high-performance tantalate photocatalysts.

The Brunauer−Emmett−Teller (BET) surface areas of the KNTO nanooctahedra and nanosheets are 12.38 and 11.42 m^2 g^{-1}, respectively, suggesting that the difference in photocatalytic activities of the two KNTO samples should not be attributed to the variations in surface area. Moreover, crystallinity can also affect the photocatalytic activity of H_2 production. The intensity of the XRD pattern of KNTO octahedra is higher than that of KNTO nanosheets as shown in Figure 1a, indicating better crystallinity of the nanooctahedra. However, the sharp XRD peaks in Figure 1a and the TEM data shown in Figures 3 and 4 confirm that both of the crystals are of good crystallinity. To further improve the crystallinity, the obtained KNTO nanosheets are dispersed in 70 mL of water and further treated under hydrothermal conditions at 180 °C for another 2 h (denoted as KNTO-180-2) considering that the crystallinity can be carefully controlled by calcination temperature and time.[14] Figure 7a,b displays the XRD pattern and SEM image of

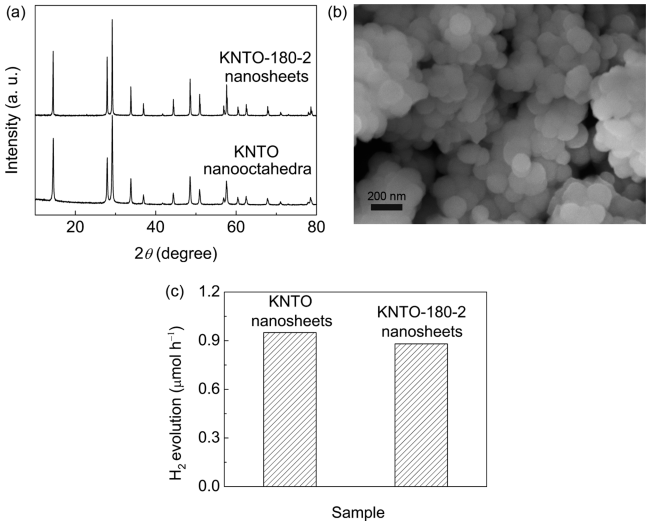

Figure 7. (a) XRD patterns of the KNTO nanooctahedra and KNTO-180-2 nanosheets. (b) FESEM image of KNTO-180-2 nanosheets. (c) Hydrogen evolution rate for the KNTO nanosheets before and after hydrothermal treatment.

the KNTO-180-2 nanosheets. After such hydrothermal treatment, the intensity of the XRD pattern of KNTO nanosheets is almost identical to the nanooctahedra as shown in Figure 7a, suggesting that the crystallinity of the two samples are similar. From the representative SEM image of the KNTO-180-2 nanosheets (Figure 7b), it can be seen that the size and morphology of the sample do not change obviously after hydrothermal treatment. The specific surface area of KNTO-180-2 nanosheets is 9.91 m^2 g^{-1}, which is a little lower than the sample before hydrothermal treatment. To evaluate the effect of crystallinity on the photocatalytic performance, photocatalytic water splitting over KNTO-180-2 was carried out under identical reaction conditions for KNTO nanocystals, and the H_2 evolution rate is shown in Figure 7c. The KNTO-180-2 sample shows a slightly lower photocatalytic activity with the H_2 evolution rate of 0.88 μmol h^{-1}, which can be explained by the decrease in the specific surface area after hydrothermal treatment. Therefore, it can be concluded that the crystallinity should not be the key factor to make the activity difference between KNTO nanooctahedra and nanosheets. On the basis

of the above observations, the main difference between the two samples is the exposed facets, which determine the surface atomic and electronic band structures[13] and thereby critically affect photocatalytic activity in general.[30] Consequently, it is speculated that the difference in the geometric structure between the KNTO nanooctahedra and nanosheets is responsible for their different photocatalytic activities for H_2 production from water splitting.

The bandgap energies for the KNTO crystals with different crystal facets were derived from UV−vis diffuse reflectance spectra as shown in Figure 8a. The sharp absorption edge

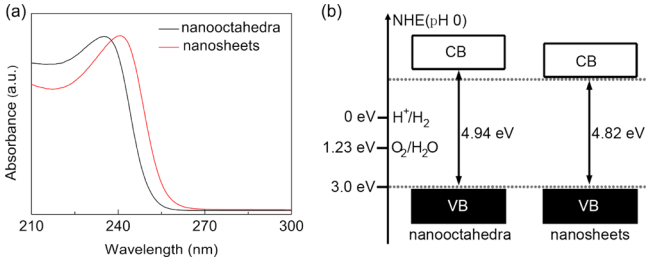

Figure 8. (a) UV−vis diffuse reflectance spectra and (b) determined valence-band and conduction-band edges of the KNTO nanooctahedra and nanosheets.

shows a small red shift from 251 nm (4.94 eV) to 257 nm (4.82 eV) as the morphology changes from nanooctahedra to nanosheets. The difference in electronic structure is probably caused by the exposure of different facets because each facet owns its own unique surface atomic arrangement which plays an important role in surface electronic configuration.[14] The band structures of the KNTO photocatalysts are shown in Figure 8b. The conduction band minimum (CBM) of the sample was estimated by the bandgap derived from Figure 8a and the valence band maxima (VBM) that were supposed to be +3.0 eV.[31,32] It can be seen that the CBM of KNTO nanooctahedra is ∼0.12 eV higher than that of spherical nanosheets. In principle, the reduction power of a photocatalyst is related to its CBM position.[33] Higher CBM gives rise to more reductive photogenerated electrons. It is therefore expected that the photoelectrons generated in the conduction band of {111}-facet-bounded nanooctahedra possess a stronger reduction power than that of nanosheets dominated with {101} facets, which is beneficial for the photocatalytic reaction. Although the difference in chemical potential between KNTO nanooctahedra and nanosheets is small, it can still serve as a key factor for the photoreactivity difference, which is similar to that for TiO_2 crystals as reported in the literature.[13,14,33] Therefore, compared to the KNTO nanosheets, the nanooctahedra show significantly higher photoactivity due to that more strongly reductive electrons generated on {111} facets can reduce H^+ into H_2 more efficiently in the photocatalytic reaction.[34]

It is generally accepted that the particular surface atom arrangement and coordination of the exposed crystal facets also play a critical role in determining the photocatalytic activities of single-crystal semiconductors.[35−37] The representative relaxed atomic models of {111} and {101} facets of KNTO are shown in Figure 9, indicating that both facets present either a positively charged K (or Na) and Ta or negatively charged O termination layer on the surface. For the positively charged layer, both facets are entirely constituted by K (or Na) and three-fold-coordinated Ta atoms with three dangling bonds

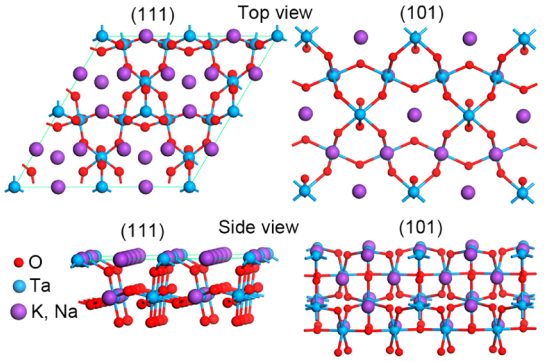

Figure 9. Side and top views of {111} and {101} surface terminations of KNTO.

(denoted as Ta_{3c}). Conventionally, the unsaturated cations can offer catalytically active sites and the facets with a higher percentage of undercoordinated atoms are usually more reactive.[8,13] The density of Ta_{3c} on {111} facets (about 2.1 atoms nm^{-2}) is lower than that on {101} facets (about 2.5 atoms nm^{-2}). On the basis of conventional understanding, the activity of {101} should be higher than that of {111}, which is not the case in the present study. A similar phenomenon for TiO_2 has been reported, where a cooperative mechanism of surface atomic structure (the density of undercoordinated Ti atoms) and surface electronic structure (the power of photoexcited charge carriers) is proposed as the determining factor for photoreactivity.[13] This mechanism can be applied to explain the unusual facet-dependent photoactivities of KNTO nanocrystals. Nevertheless, more efforts are needed to further clarify the underlying mechanism for the facet-dependent performance because of the complexity of KNTO crystal in composition and structure. At this stage, it is reasonable to conclude that the photocatalytic water splitting activities of the obtained KNTO crystals are tuned by their exposed facets, and compared to the {101} facets, the {111} facets are more reactive and can accelerate the redox reactions.

4. CONCLUSIONS

In summary, a novel two-step synthetic approach has been developed for the controlled synthesis of KNTO at a relatively low temperature. By varying the amount of KOH added in the hydrothermal process, two distinct KNTO nanocrystals, {111}-terminated octahedra and {101}-dominated nanosheets, can be selectively prepared. Interestingly, the as-obtained crystals show high activity in photocatalytic H_2 evolution from CH_3OH/H_2O solution, and their performances mainly depend on the exposed facets. The rate of H_2 evolution under UV−light irradiation is about 4.4 μmol h^{-1} for the KNTO nanooctahedra, which is 3 times higher than that of KNTO nanosheets dominantly exposed with {101} facets. The facet-dependent activities can be attributed to a cooperative effect of surface atomic structure (the density of undercoordinated Ta atoms) and electronic structure (the position of conduction band minimum).

AUTHOR INFORMATION

Corresponding Author

*E-mail: cywang@ms.xjb.ac.cn.

Notes

The authors declare no competing financial interest.

■ ACKNOWLEDGMENTS

This work was supported by the Excellent Youth Foundation of Xinjiang Uygur Autonomous Region (2013711004), the National Nature Science Foundation of China (Grant Nos. 21011113, 21173261), the "One Hundred Talents Project Foundation Program" of Chinese Academy of Sciences, International Science & Technology Cooperation Program of Xinjiang Uygur Autonomous Region (20116010), the "Cross-Cooperation Program for Creative Research Teams" of Chinese Academy of Sciences, and the "Western Light" Program of Chinese Academy of Sciences (XBBS200916). The authors also gratefully acknowledge financial support from "Key Laboratory of Photochemical Conversion and Optoelectronic Materials,TIPC, CAS" (PCOM201220).

■ REFERENCES

(1) Tian, N.; Zhou, Z. Y.; Sun, S. G.; Ding, Y.; Wang, Z. L. *Science* **2007**, *316*, 732−735.
(2) Yin, Y. D.; Alivisators, A. P. *Nature* **2005**, *437*, 664−670.
(3) Gou, X. L.; Cheng, F. Y.; Shi, Y. H.; Zhang, L.; Peng, S. J.; Chen, J.; Shen, P. W. *J. Am. Chem. Soc.* **2006**, *128*, 7222−7229.
(4) Lin, J.; Lin, J.; Zhu, Y. F. *Inorg. Chem.* **2007**, *46*, 8372−8378.
(5) Yang, H. G.; Sun, C. H.; Qiao, S. Z.; Zou, J.; Liu, G.; Smith, S. C.; Cheng, H. M.; Lu, G. Q. *Nature* **2008**, *453*, 638−641.
(6) Bi, Y. P.; Ouyang, S. X.; Umezawa, N. T.; Cao, J. Y.; Ye, J. H. *J. Am. Chem. Soc.* **2011**, *133*, 6490−6492.
(7) Jiang, J.; Zhao, K.; Xiao, X. Y.; Zhang, L. Z. *J. Am. Chem. Soc.* **2012**, *134*, 4473−4476.
(8) Zhou, X. M.; Lan, J. Y.; Liu, G.; Deng, K.; Yang, Y. L.; Nie, G. J.; Yu, J. G.; Zhi, L. J. *Angew. Chem., Int. Ed.* **2012**, *51*, 178−182.
(9) Zhang, L.; Chen, D. R.; Jiao, X. L. *J. Phys. Chem. B* **2006**, *110*, 2668−2673.
(10) Huang, W. C.; Lyu, L. M.; Yang, Y. C.; Huang, M. H. *J. Am. Chem. Soc.* **2012**, *134*, 1261−1267.
(11) Xi, G. C.; Ye, J. H. *Chem. Commun.* **2010**, *46*, 1893−1895.
(12) Lou, Z. Z.; Huang, B. B.; Qin, X. Y.; Zhang, X. Y.; Cheng, H. F.; Liu, Y. Y.; Wang, S. Y.; Wang, J. P.; Dai, Y. *Chem. Commun.* **2012**, *48*, 3488−3490.
(13) Pan, J.; Liu, G.; Lu, G. Q.; Cheng, H. M. *Angew. Chem., Int. Ed.* **2011**, *50*, 2133−2137.
(14) Xu, H.; Reunchan, P.; Ouyang, S. X.; Tong, H.; Umezawa, N.; Kako, T.; Ye, J. H. *Chem. Mater.* **2013**, *25*, 405−411.
(15) Gordon, T. R.; Cargnello, M.; Paik, T.; Mangolini, F.; Weber, R. T.; Fornasiero, P.; Murray, C. B. *J. Am. Chem. Soc.* **2012**, *134*, 6751−6761.
(16) Jiao, W.; Wang, L. Z.; Liu, G.; Lu, G. Q.; Cheng, H. M. *ACS Catal.* **2012**, *2*, 1854−1859.
(17) Osterloh, F. E. *Chem. Mater.* **2008**, *20*, 35−54.
(18) Sun, J. Q.; Chen, G.; Li, Y. X.; Jin, R. C.; Wang, Q.; Pei, J. *Energy Environ. Sci.* **2011**, *4*, 4052−4060.
(19) Maeda, K.; Domen, K. *Angew. Chem., Int. Ed.* **2012**, *51*, 9865−9869.
(20) Zou, Z. G.; Ye, J. H.; Sayama, K.; Arakawa, H. *Nature* **2001**, *414*, 625−627.
(21) Kato, H.; Asakura, K.; Kudo, A. *J. Am. Chem. Soc.* **2003**, *125*, 3082−3089.
(22) Zhou, C.; Chen, G.; Li, Y. X.; Zhang, H. J.; Pei, J. *Int. J. Hydrogen Energy* **2009**, *34*, 2113−2120.
(23) Liu, J. W.; Chen, G.; Li, Z. H.; Zhang, Z. G. *Int. J. Hydrogen Energy* **2007**, *32*, 2269−2272.
(24) Li, Y. X.; Chen, G.; Zhou, C.; Sun, J. X. *Chem. Commun.* **2009**, 2020−2022.
(25) Xu, T. G.; Zhang, C.; Shao, X.; Wu, K.; Zhu, Y. F. *Adv. Funct. Mater.* **2006**, *16*, 1599−1607.
(26) Xu, T.; Zhao, X.; Zhu, Y. F. *J. Phys. Chem. B* **2006**, *110*, 25825−25832.
(27) Duan, N. G.; Tian, Z. R.; Willis, W. S.; Suib, S. L.; Newsam, J. M.; Levine, S. M. *Inorg. Chem.* **1998**, *37*, 4697−4701.
(28) Goh, G. K. L.; Haile, S. M.; Levi, C. G.; Lange, F. F. *J. Mater. Res.* **2002**, *17*, 3168−3176.
(29) Hosono, E.; Fujihara, S.; Imai, H.; Honma, I.; Masaki, I.; Zhou, H. C. *ACS Nano* **2007**, *1*, 273−278.
(30) Hoffmann, M. R.; Martin, S. T.; Choi, W.; Bahnemann, D. W. *Chem. Rev.* **1995**, *95*, 69−96.
(31) Miseki, Y.; Kato, H.; Kudo, A. *Energy Environ. Sci.* **2009**, *2*, 306−314.
(32) Scaife, D. E. *Sol. Energy* **1980**, *25*, 41−54.
(33) Xu, H.; Ouyang, S.; Li, P.; Kako, T.; Ye, J. *ACS Appl. Mater. Interfaces* **2013**, *5*, 1348−1354.
(34) Tooru, I.; Akira, F.; Satoshi, K.; Kenichi, H. *Nature* **1979**, *277*, 637−638.
(35) Tong, H.; Ouyang, S. X.; Bi, Y. P.; Umezawa, N.; Oshikiri, M.; Ye, J. H. *Adv. Mater.* **2012**, *24*, 229−251.
(36) Liu, G.; Yu, J. C.; Lu, G. Q.; Cheng, H. M. *Chem. Commun.* **2011**, *46*, 6763−6783.
(37) Wang, H.; Yang, J. T.; Li, X. L.; Zhang, H. Z.; Li, J. H.; Guo, L. *Small* **2012**, *8*, 2802−2806.